International Journal of Pharmaceutics: X 10 (2025) 100348

Contents lists available at ScienceDirect

International Journal of Pharmaceutics: X

journal homepage: www.sciencedirect.com/journal/international-journal-of-pharmaceutics-x

# Synergistic photodynamic and chemodynamic therapy using hypoxia-adaptive Ce6@Co nanoparticles for enhanced tumor suppression

Yeji Chang, Yong Geun Lim, Kyeongsoon Park *

*Department of Systems Biotechnology, Chung-Ang University, Anseong, Gyeonggi 17546, Republic of Korea*

ARTICLE INFO

*Keywords:*
Chlorin e6 (Ce6)
$Co^{2+}$-mediated Ce6 self-assembly
Hypoxia-adaptive nanoplatform
Photodynamic therapy (PDT)
Chemodynamic therapy (CDT)
Hypoxic solid tumor

ABSTRACT

Conventional photodynamic therapy (PDT) is less effective in solid tumors owing to Type-II PDT mechanism's reliance on oxygen ($O_2$), which is scarce in hypoxic environments. Most hydrophobic photosensitizers have poor water solubility, complicating their formulation and delivery. To address these challenges, Ce6@Co nanoparticles (a hypoxia-adaptive nanoplatform) were developed via coordinating $Co^{2+}$ ions with chlorin e6 (Ce6), exhibiting uniform size (~230 nm), enhanced dispersibility, and colloidal stability. These nanoparticles generate dual-mode reactive oxygen species (ROS): Type-II $^1O_2$ via PDT under 670 nm irradiation and oxygen-independent hydroxyl radical (·OH) via $Co^{2+}$-mediated Fenton-like reactions. In vitro, Ce6@Co nanoparticles demonstrated superior cellular uptake and robust ROS amplification, and reduced squamous cell carcinoma (SCC7) cell viability to 34.4 % under normoxia and 20.48 % under hypoxia via synergistic photodynamic and chemodynamic (PDT-CDT) effects, causing considerable apoptosis. In vivo, intratumoral administration of Ce6@Co nanoparticles via laser irradiation completely suppressed tumors in SCC7 tumor-bearing mice. This effect was attributed to favorable intratumoral distribution, enhanced retention, and synergistic PDT-CDT. No systemic toxicity was observed, as indicated by stable body weight, normal serum biomarkers, and unchanged organ histology. The $Co^{2+}$-coordinated photosensitizer system uses hypoxia-elevated $H_2O_2$ to sustain CDT, effectively overcoming conventional PDT's oxygen dependence and offering a safe and effective dual-modal therapeutic strategy for hypoxic solid tumors.

## 1. Introduction

Photodynamic therapy (PDT) uses photosensitizers (PSs) to generate cytotoxic singlet oxygen ($^1O_2$) via a Type-II mechanism, selectively targeting malignant tumor cells under light activation in oxygenated environments (Alsaab et al., 2020; Huis In't Veld et al., 2023; Lan et al., 2019). Although effective in normoxic conditions, this oxygen-dependent process faces critical limitations in hypoxic tumor microenvironments (TME) owing to restricted $^1O_2$ production, and diminishes therapeutic efficacy (An et al., 2022; Gunaydin et al., 2021; Lan et al., 2019). PDT also consumes molecular oxygen ($O_2$) during irradiation, exacerbating hypoxia and triggering adverse outcomes such as tumor angiogenesis and metastasis (Chai et al., 2023; Wei et al., 2021). This oxygen depletion occurs when photochemical $O_2$ consumption exceeds the rate of diffusion from vasculature, particularly in poorly perfused solid tumors (An et al., 2022).

Various PSs, including porphyrins, chlorins, phthalocyanines, synthetic dyes, metal complexes, and natural products, are used in biomedical applications, particularly PDT in cancer and infectious diseases (Abrahamse and Hamblin, 2016; Correia et al., 2021; Escudero et al., 2021; Wen et al., 2024). Among them, chlorin e6 (Ce6), a second-generation PS, has attracted attention for PDT use in cancer and other biomedical applications (Hak et al., 2023; Kim and Chang, 2023). Ce6 has a high $^1O_2$ quantum yield, strong near-infrared absorption for deeper tissue penetration, and a favorable safety profile (Hak et al., 2023; Kim and Chang, 2023; Yu et al., 2025). It also shows efficacy beyond oncology, including anti-inflammatory therapy and fluorescence-guided procedures (Liao et al., 2023; Yu et al., 2025). However, the biomedical application of Ce6 is hindered by its intrinsic hydrophobicity, complicating formulation and leading to poor biodistribution (Hak et al., 2023; Kim and Chang, 2023).

Alternative strategies have been developed to address the oxygen dependency of PDT in hypoxic TME. These approaches include the use of cyclic nanoreactors that initiate ROS cascade reactions, as well as oxygen-generating nanosystems designed to locally increase $O_2$ concentrations or inhibit hypoxia-inducible signaling pathways, thereby

* Corresponding author.
*E-mail address:* kspark1223@cau.ac.kr (K. Park).

https://doi.org/10.1016/j.ijpx.2025.100348
Received 18 May 2025; Received in revised form 12 June 2025; Accepted 19 June 2025
Available online 20 June 2025

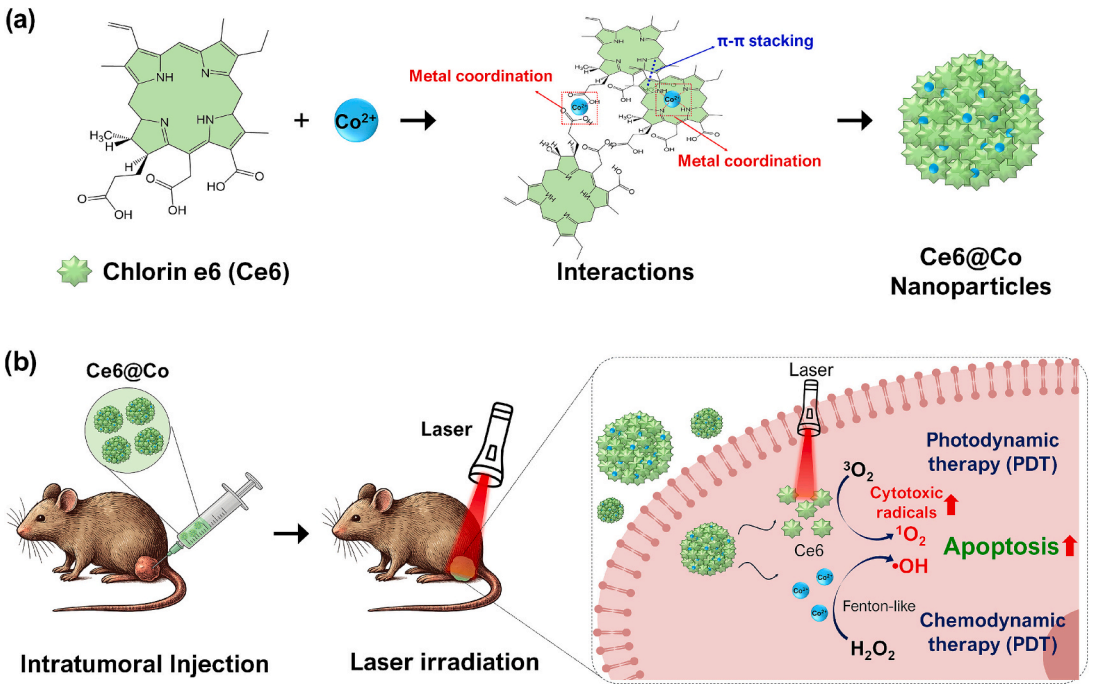


**Scheme 1.** A schematic depicting a hypoxia-adaptive nanoplatform based on $Co^{2+}$-coordinated Ce6 (Ce6@Co) nanoparticles for dual-modal photodynamic and chemodynamic cancer therapy. (a) The hypoxia-adaptive $Co^{2+}$-coordinated Ce6 (Ce6@Co) nanoparticles are constructed by coordinating $Co^{2+}$ ions with Ce6 via metal ion coordination and additional π-π stacking interactions. (b) Following intratumoral injection in SCC7 tumor-bearing mice, Ce6@Co nanoparticles distribute throughout the tumor tissue, generating $^1O_2$ via Type-II PDT under 670 nm laser irradiation and simultaneously producing cytotoxic ·OH via $Co^{2+}$-mediated Fenton-like reactions, even in the hypoxic TME. This amplified dual-ROS generation induces significant apoptosis and results in effective tumor regression.

improving PDT efficacy under hypoxia. While most of these methods focus on restoring or supplementing oxygen levels, our approach employs a therapeutic strategy that functions independently of oxygen availability, offering a more robust and reliable solution for treating hypoxic tumors (Liu et al., 2019; Liu et al., 2021). Chemodynamic therapy (CDT) is a reactive oxygen species (ROS)-dependent anticancer approach leveraging transition metal ions (e.g., $Fe^{2+}$, $Co^{2+}$, $Mn^{2+}$, and $Cu^{2+}$) to catalyze Fenton-type reactions within the TME, converting endogenous hydrogen peroxide ($H_2O_2$) into highly cytotoxic hydroxyl radicals (·OH) without oxygen dependency (Jia et al., 2022; Zhang et al., 2016). Unlike oxygen-reliant PDT, CDT exploits tumor-overexpressed $H_2O_2$ (50–100 μM) to maintain ·OH production under hypoxia, causing selective oxidative damage in cancer cells while minimizing off-target effects due to low levels of $H_2O_2$ in healthy tissues (Cheng et al., 2019; Yi et al., 2024). Concurrently, metal ion coordination addresses Ce6's intrinsic hydrophobicity: its porphyrin-derived structure containing a conjugated macrocycle and three carboxylic acid groups enables stable chelation with transition metal ions such as $Fe^{3+}$, $Cu^{2+}$, and $Zn^{2+}$ (Balem et al., 2009; Leshem et al., 2019; Pei et al., 2023), enhancing aqueous solubility and colloidal stability. Structural analyses confirm that transition metal ions such as $Fe^{2+}$, $Mn^{3+}$, $Pd^{2+}$, and $Co^{2+}$ can be coordinately embedded within the macrocyclic ring of chlorin and porphyrin PSs, enhancing photostability via heavy-atom effects and optimizing photoactivity through symmetry-mediated electronic reorganization (Lee et al., 2023; Song et al., 2011).

Based on these CDT principles via Fenton or Fenton-like reactions, and metal ion coordination chemistry, we hypothesize that a hypoxia-adaptive nanoplatform based on metal ion-coordinated Ce6 nanoparticles overcomes the conventional PDT's critical limitations in solid tumors such as oxygen dependency and PS intrinsic hydrophobicity. Among transition metal ions, $Co^{2+}$ exhibits high catalytic activity for converting $H_2O_2$ to ·OH via Fenton-like reactions (Liu et al., 2017b; Park et al., 2023; Zhang et al., 2019), and can effectively coordinate with Ce6 (Lee et al., 2023; Song et al., 2011). This study developed a hypoxia-adaptive nanoplatform composed of $Co^{2+}$-coordinated Ce6 (Ce6@Co) nanoparticles by coordinating $Co^{2+}$ ion with Ce6 using metal-coordination and π-π stacking (Scheme 1a). Importantly, Ce6@Co nanoparticles integrate dual therapeutic modalities: they generate $^1O_2$ via Type-II PDT under 670 nm laser irradiation and simultaneously produce cytotoxic ·OH through $Co^{2+}$-mediated Fenton-like reactions, thereby enabling robust ROS amplification even in hypoxic TME (Scheme 1b). Ce6@Co nanoparticles' rational design thus represents a novel and effective strategy for overcoming PDT's oxygen-dependent limitations and offers a promising and safe dual-modal therapeutic platform for hypoxic solid tumors.

## 2. Materials and methods

### 2.1. Materials

Ce6 was procured from Frontier Scientific, Inc. (Logan, UT, USA). Cobalt(II) chloride ($CoCl_2$), Tween 20, potassium bromide (KBr), 2′,7′-dichlorofluorescein diacetate (DCFDA), deuterated chloroform ($CDCl_3$), deuterated dimethyl sulfoxide (DMSO-$d_6$), hydrogen peroxide solution ($H_2O_2$, 30 % *w*/w), terephthalic acid (TA), and cobalt standard solution for inductively coupled plasma (ICP) spectrometric analysis were obtained from Sigma-Aldrich (St. Louis, MO, USA). Analytical-grade dimethyl sulfoxide (DMSO, 99.5 %) was purchased from SAMCHUN Pure Chemicals (Pyeongtaek, Korea). Dialysis membranes with a molecular weight cut-off (MWCO) of 1 kDa were acquired from Spectrum Laboratories (Rancho Dominguez, CA, USA). Phosphate-buffered saline (PBS) was sourced from Lonza (Walkersville, MD, USA). Roswell Park Memorial Institute 1640 medium (RPMI 1640), fetal bovine serum (FBS), and Dulbecco's phosphate-buffered saline (DPBS) were purchased from Welgene Inc. (Pyeongtaek, Korea). The Cell Counting Kit-8 (CCK-8) was obtained from Dojindo Molecular Technologies (Kumamoto, Japan), and the CF®488 A Annexin V/propidium iodide (PI) apoptosis detection kit was sourced from Biotium Inc. (Fremont, CA, USA). Singlet Oxygen Sensor Green (SOSG) was acquired from Thermo Fisher Scientific (Waltham, MA, USA).

### 2.2. Synthesis and characterization of Ce6@Co nanoparticles

Ce6 (30 mg, 0.05 mmol) and $CoCl_2$ (65 mg, 0.5 mmol) were solubilized in DMSO (10 mL), and this mixture underwent magnetic stirring for 24 h to facilitate $Co^{2+}$-Ce6 coordination. The reaction solution was then dialyzed (MWCO: 1 kDa) against deionized water (DW) for 72 h. This purification step removed unreacted $Co^{2+}$ ions and residual DMSO, inducing nanoparticle self-assembly through metal-ligand coordination and π-π stacking. The purified Ce6@Co nanoparticle dispersion was stored at 4 °C. Free Ce6 was prepared under identical synthesis conditions via the same coordination-driven protocol, without $CoCl_2$, as a control to elucidate the role of cobalt coordination in nanoparticle self-assembly. Prior to experimental use, the nanoparticle stock solution was sonicated via probe ultrasonication (Ultrasonic Processor KFS-150 N, Korea Process Technology Co., Ltd., Seoul, Korea) at 12 W for 5 min to ensure monodispersion and colloidal stability.

The photosensitizer content of Ce6@Co nanoparticles was quantified by analyzing Ce6 concentrations derived from a calibration curve [$Y = 54.725\times + 0.0143$ ($R^2 = 0.9995$)] using UV/Vis spectrophotometry ($\lambda = 670$ nm). $Co^{2+}$ ion content within the nanoparticles was quantified by inductively coupled plasma optical emission spectrometry (ICP-OES; Optima 5300 DV, PerkinElmer, USA) following concentrated nitric acid ($HNO_3$) and hydrogen peroxide ($H_2O_2$) treatment.

To confirm the successful synthesis of Ce6@Co nanoparticles, structural analysis was performed using $^1$H NMR spectroscopy (VNS 600 MHz, Varian, Palo Alto, CA, USA) at a concentration of 5 mg/mL in $CDCl_3$. For comparison, the free Ce6 control sample was analyzed in DMSO-$d_6$. Fourier transform infrared spectroscopy (FT-IR; Shimadzu 8400S, Kyoto, Japan) identified cobalt-coordination shifts in functional groups. The hydrodynamic mean size, *Z*-average size, and polydispersity index (PDI) of the free Ce6 control sample and Ce6@Co nanoparticles were determined via dynamic light scattering (DLS, SZ-100, Horiba, Kyoto, Japan). Zeta potential analysis of free Ce6 sample and Ce6@Co nanoparticles was conducted using a Zetasizer (Malvern Panalytical Ltd., Malvern, UK).

Aqueous dispersibility of Ce6@Co nanoparticles and free Ce6 was compared via photographs taken before and after probe sonication (12 W, 5 min) to assess colloidal stability using an Ultrasonic Processor. Additionally, to evaluate colloidal stability under storage conditions, free Ce6 and Ce6@Co nanoparticles were diluted 20-fold in DW, PBS (pH 7.4), and DMEM containing 10 % FBS (10 % FBS). Samples were stored at 4 °C, and their hydrodynamic Z-average sizes were monitored using dynamic light scattering (SZ-100) at intervals of 0, 1, 5, 7, 10, 14, 21, and 28 d. Morphological analysis was performed via field-emission transmission electron microscopy (FE-TEM, JEM-F200, JEOL, Tokyo, Japan). $Co^{2+}$ ion presence within nanoparticles was confirmed via energy-dispersive X-ray spectroscopy (EDS) elemental mapping. To confirm nanosized assembly, free Ce6 in DMSO and Ce6@Co nanoparticles in both water and DMSO were analyzed to compare absorbance profiles using UV/Vis spectrophotometry (NEO-S490P, Neogen Inc., Daejeon, Korea).

### 2.3. $^1O_2$ and ·OH generation ability of Ce6@Co nanoparticles

$^1O_2$ generation via Ce6@Co nanoparticles following laser irradiation was assessed by monitoring SOSG fluorescence intensity. Three sample groups were prepared: (1) free Ce6 (5 μM) in pH 7.4 PBS with 1 % Tween 20, (2) Ce6@Co nanoparticles (equivalent Ce6 concentration: 5 μM) in pH 7.4 PBS with 1 % Tween 20, and (3) Ce6@Co nanoparticles (equivalent Ce6 concentration: 5 μM) in pH 7.4 PBS without Tween 20. The fluorescence emission spectra of the three samples were measured using a fluorescence spectrometer (FS-2, Scinco, Seoul, Korea). For determining $^1O_2$ generation, SOSG (1 μM; excitation/emission: 504/525 nm) was added to each sample. Fluorescence intensity was measured using a fluorescence spectrometer (FS-2, Scinco, Seoul, Korea) following irradiation using a 670 nm laser at 50 mW/cm$^2$ for time intervals ranging from 0 to 120 s.

·OH generation via Ce6@Co nanoparticles was evaluated using TA as a fluorescence probe. Five experimental groups were prepared as follows: (1) 2 mM TA alone, (2) free Ce6 (20 μM) with 2 mM TA, (3) free Ce6 (20 μM) with 2 mM TA and 500 μM $H_2O_2$, (4) Ce6@Co nanoparticles (equivalent Ce6 concentration: 20 μM) with 2 mM TA, and (5) Ce6@Co nanoparticles (equivalent Ce6 concentration: 20 μM) with 2 mM TA and 500 μM $H_2O_2$. Each solution was incubated at 25 °C for 7 d. The fluorescence spectra of TA were recorded using a fluorescence spectrometer with an excitation wavelength of 310 nm and emission measured in the range of 400–540 nm.

### 2.4. In vitro cellular uptake, intracellular ROS levels in normoxia and hypoxia, and dark toxicity

Squamous cell carcinoma (SCC7) cells were obtained from American Type Culture Collection (Rockville, MD, USA), while human dermal fibroblast (HDF) cells were sourced from Lonza (Basel, Switzerland). SCC7 cells were cultured in RPMI 1640, while HDF cells were maintained in DMEM. Both media were supplemented with 10 % FBS and 1 % penicillin-streptomycin. All cells were incubated at 37 °C in a humidified 5 % $CO_2$ atmosphere.

To assess the intracellular uptake of free Ce6 and Ce6@Co nanoparticles, SCC7 cells ($1 \times 10^4$ cells/well) were seeded in 4-well cell culture plates and incubated for 24 h. Subsequently, the cells were exposed to either free Ce6 or Ce6@Co nanoparticles at various Ce6 concentrations (0, 2.5, 5, and 10 μM) for an additional 24 h. Thereafter, the cells were carefully washed three times with DPBS and fixed with 3.7 % (*v*/v) formaldehyde at 25 °C for 30 min. Cell nuclei were counterstained with 4′,6′-diamidino-2-phenylindole hydrochloride (DAPI; SouthernBiotech, AL, USA). Intracellular localization and free Ce6 and Ce6@Co nanoparticle uptake were visualized using a custom-built confocal laser scanning fluorescence microscope (CLSM). Cellular fluorescence was quantified by measuring the corrected total cell fluorescence (CTCF) of Ce6 in selected cells from CLSM images. ImageJ software (Ver 1.53a, NIH, MD, USA) was used for analysis based on Formula (1) (Lim et al., 2025; Nguyen et al., 2024).

$$\text{CTCF} = \text{Integrated density} - (\text{Area of selected cell} \times \text{Mean fluorescence signal of background readings}) \quad (1)$$

To compare intracellular $H_2O_2$ levels in SCC7 cells cultured under normoxic and hypoxic conditions, SCC7 cells ($1 \times 10^4$ cells/well) were seeded into 4-well culture plates and incubated for 24 h under either normoxic conditions (a humidified 5 % $CO_2$ incubator) or hypoxic conditions (a $N_2$-gas-purged, custom-made hypoxic chamber), as previously described (Min et al., 2021). Following incubation, the cells were treated with 2′,7′-dichlorofluorescein diacetate (DCFDA, 10 μM) at 37 °C for 30 min to allow for intracellular $H_2O_2$ detection. Then, the cells were carefully washed with DPBS, fixed with 3.7 % (*v*/v) formaldehyde for 30 min at 25 °C, and cell nuclei were counterstained with DAPI (SouthernBiotech). Intracellular $H_2O_2$ levels were visualized using CLSM, and fluorescence intensities were quantitatively analyzed using ImageJ software to compare the oxidative status of cells under normoxic versus hypoxic conditions.

For the evaluation of dark toxicity, SCC7 and HDF cells ($5 \times 10^3$ cells/well) were seeded into black 96-well culture plates and incubated for 24 h. Subsequently, the cells were treated with either free Ce6 or Ce6@Co nanoparticles at various Ce6 concentrations (0, 2.5, 5, 10, and 20 μM) for an additional 24 h. After treatment, the cells were carefully washed three times with DPBS. Cell viability was assessed using the CCK-8 (Dojindo Laboratories) assay according to the manufacturer's protocols. The absorbance was measured at 450 nm using a microplate reader (Multiskan Go, Thermo Fisher Scientific). Cell viability was calculated as the percentage ratio of absorbance in treated groups relative to the untreated control group, reflecting the proportion of

viable cells under non-irradiated dark conditions.

### 2.5. In vitro therapeutic effects of Ce6@Co nanoparticles under normoxic and hypoxic conditions

SCC7 cells ($5 \times 10^3$ cells/well) seeded in black 96-well culture plates were prepared under either normoxic or hypoxic conditions as described in the "*In vitro intracellular $H_2O_2$ levels of SCC7 cells under normoxia and hypoxia*" section. The cells were subsequently treated with free Ce6 and Ce6@Co nanoparticles at final Ce6 concentrations of 0 or 5 μM for 24 h. After treatment, cells were thoroughly washed with DPBS. Thereafter, cells were subjected to irradiation using a 670 nm laser at 50 mW/cm$^2$ for 30 s or maintained in the absence of light as non-irradiated controls, and subsequently incubated for an additional 24 h. After incubation, the cells were washed again with DPBS and incubated at 37 °C with CCK-8 reagent for 4 h to evaluate cell viability. The absorbance was measured at 450 nm using a microplate reader (Multiskan Go), and cell viability was determined by comparing the absorbance of treated groups to that of untreated control groups.

To comparatively assess intracellular ROS levels in SCC7 cells treated with Ce6@Co nanoparticles under normoxic conditions or hypoxic conditions post-laser irradiation, SCC7 cells ($3 \times 10^4$ cells/well) were seeded in 4-well culture plates, and further incubated at 37 °C for 24 h under either normoxic conditions (humidified 5 % $CO_2$ incubator) or hypoxic conditions ($N_2$-purged chamber). After incubation, the cells were treated with Ce6@Co nanoparticles at an equivalent Ce6 concentration of 5 μM for 24 h. Following treatment, the cells were washed three times with DPBS. Subsequently, they were either exposed to a 670 nm laser (50 mW/cm$^2$) for 30 s or maintained as non-irradiated controls, followed by a 24 h incubation. The cells were subsequently washed with DPBS and incubated with 10 μM of DCFDA for 30 min to detect intracellular ROS. After staining, the cells were fixed with 3.7 % (*v*/v) formaldehyde at 25 °C for 30 min and nuclei were counterstained with DAPI. Intracellular $H_2O_2$ levels were visualized using CLSM. The CTCF of oxidized DCF (a ROS-specific product) was quantified from CLSM images using ImageJ software.

Annexin V and PI staining assessed early and late apoptosis in SCC7 cells treated with free Ce6 or Ce6@Co nanoparticles under normoxic and hypoxic conditions following laser irradiation. SCC7 cells ($5 \times 10^3$ cells/well) were seeded in 8-well culture plates and incubated at 37 °C for 24 h under either normoxic conditions (humidified 5 % $CO_2$ incubator) or hypoxic conditions ($N_2$-purged chamber). Subsequently, the cells were treated with free Ce6 or Ce6@Co nanoparticles at final Ce6 concentrations of 0 or 5 μM for 24 h. After treatment, the culture medium was aspirated, and the cells were washed three times with DPBS. Thereafter, the cells were either exposed to a 670 nm laser (50 mW/cm$^2$) for 30 s or maintained as non-irradiated controls. Following an additional 24 h incubation, the cells were washed with DPBS and stained with CF® 488 A Annexin V and PI at 25 °C for 30 min, according to the manufacturer's protocol. After staining, the cells were washed again with DPBS and fixed with 3.7 % (v/v) formaldehyde at 25 °C for 30 min, and nuclei were counterstained with DAPI. Early and late apoptosis were visualized using CLSM. The CTCF of Annexin V and PI was quantified from CLSM images using ImageJ software.

### 2.6. In vivo antitumor effects of Ce6@Co nanoparticles

All in vivo animal studies were approved by the Institutional Animal Care and Use Committee of Chung-Ang University (202401030072). All procedures were conducted in accordance with the National Research Council's Guide for the Care and Use of Laboratory Animals. To establish a subcutaneous tumor model, SCC7 cells ($1 \times 10^6$ cells/mouse) were injected into the flank of 7-week-old female C3H mice (Doo Yeol Biotech, Seoul, Korea). In vivo experiments were initiated when tumor volumes reached 100–150 mm$^3$, as calculated using the formula: tumor volume = 0.5 × length × width$^2$.

When tumors reached the predefined volume of 100–150 mm$^3$, SCC7 tumor-bearing mice were randomly assigned into four groups: PBS control ($n = 5$), free Ce6 with laser irradiation (n = 5), Ce6@Co nanoparticles without laser irradiation (n = 5), and Ce6@Co nanoparticles with laser irradiation (n = 5). Each group was administered an intratumoral injection of either PBS, free Ce6 (1 mg/kg), or Ce6@Co nanoparticles (an equivalent Ce6 dose of 1 mg/kg). In the two groups designated for PDT, tumors were irradiated with a 670 nm laser at 100 mW/cm$^2$ for 20 min. Based on previous studies demonstrating that intratumorally administered PSs or fluorescent-labeled nanoparticles exhibit strong and persistent tumor fluorescence at 6 h post-injection (Badiee et al., 2022; Ma et al., 2021a), laser irradiation was performed 6 h post-Ce6 or Ce6@Co nanoparticle injection. Tumor volumes were recorded daily using digital calipers. On day 10 post-treatment, tumors were excised, weighed, and subsequently fixed in 10 % buffered formalin (Formalin solution, neutral buffered, 10 %, Sigma-Aldrich, St. Louis, MO, USA) or embedded in paraffin wax. Additionally, intratumoral distribution and retention of free Ce6 and Ce6@Co nanoparticles were assessed following intratumoral administration, as detailed in the Supplementary Information. Tissue slices ($n = 3$ per group) were stained with hematoxylin and eosin (H&E) to assess histopathological changes. These stained tissues were observed under an automated slide scanner (MoticEasyScan Pro 6, Motic Asis Corp., Kowloon, Hong Kong). For apoptosis detection, paraffin-embedded tissue sections were subjected to the terminal deoxynucleotidyl transferase-mediated nick end labeling (TUNEL) assay (Promega Corp., WI, USA), according to manufacturer's instructions. Tumor nuclei were counterstained with DAPI. Apoptotic cell death in tissue sections was visualized and quantified using a custom-built CLSM.

### 2.7. In vivo biosafety assay

Mice body weight in all experimental groups was measured daily throughout the study to assess in vivo biosafety. On day 10 post-treatment, blood samples were collected from the inferior vena cava of mice anesthetized with isoflurane (1 %, *w/v*, JW-Pharma, Korea) in 2 L/min oxygen. Mice were subsequently euthanized, and major organs (liver, lung, spleen, kidneys, and heart) were harvested for histopathological evaluation. Serum was separated by centrifuging the collected blood at 1500 *g* for 15 min at 4 °C without adding an anticoagulant.

Serum biochemical analysis assessed organ function. Renal function was evaluated by measuring blood urea nitrogen (BUN) and creatinine (CREA) levels, whereas hepatic function was assessed by determining aspartate aminotransferase (AST), alanine transaminase (ALT), and alkaline phosphatase (ALP) levels. All biochemical parameters were quantified using an automated clinical analyzer (Hitachi 7180 Clinical Analyzer, Hitachi, Yokohama, Japan). For histological analysis, harvested organs were sectioned into 3-μm-thick slices, stained with H&E, and examined using the automated slide scanner.

### 2.8. Statistical analyses

Data are represented as the mean ± standard deviation. Comparisons between two independent groups were performed using the independent samples *t*-test. For analyses involving more than two groups, one-way analysis of variance was conducted. All statistical analyses were performed using SigmaPlot software (version 15; Chicago, IL, USA). Statistical significance was defined as $p < 0.05$, 0.01, or 0.005.

## 3. Results and discussion

### 3.1. Synthesis and characterization of Ce6@Co nanoparticles

Ce6 is a porphyrin derivative with a conjugated macrocycle and three carboxylic acid groups that enable coordination with transition metal ions (Balem et al., 2009; Lee et al., 2023; Leshem et al., 2019; Pei

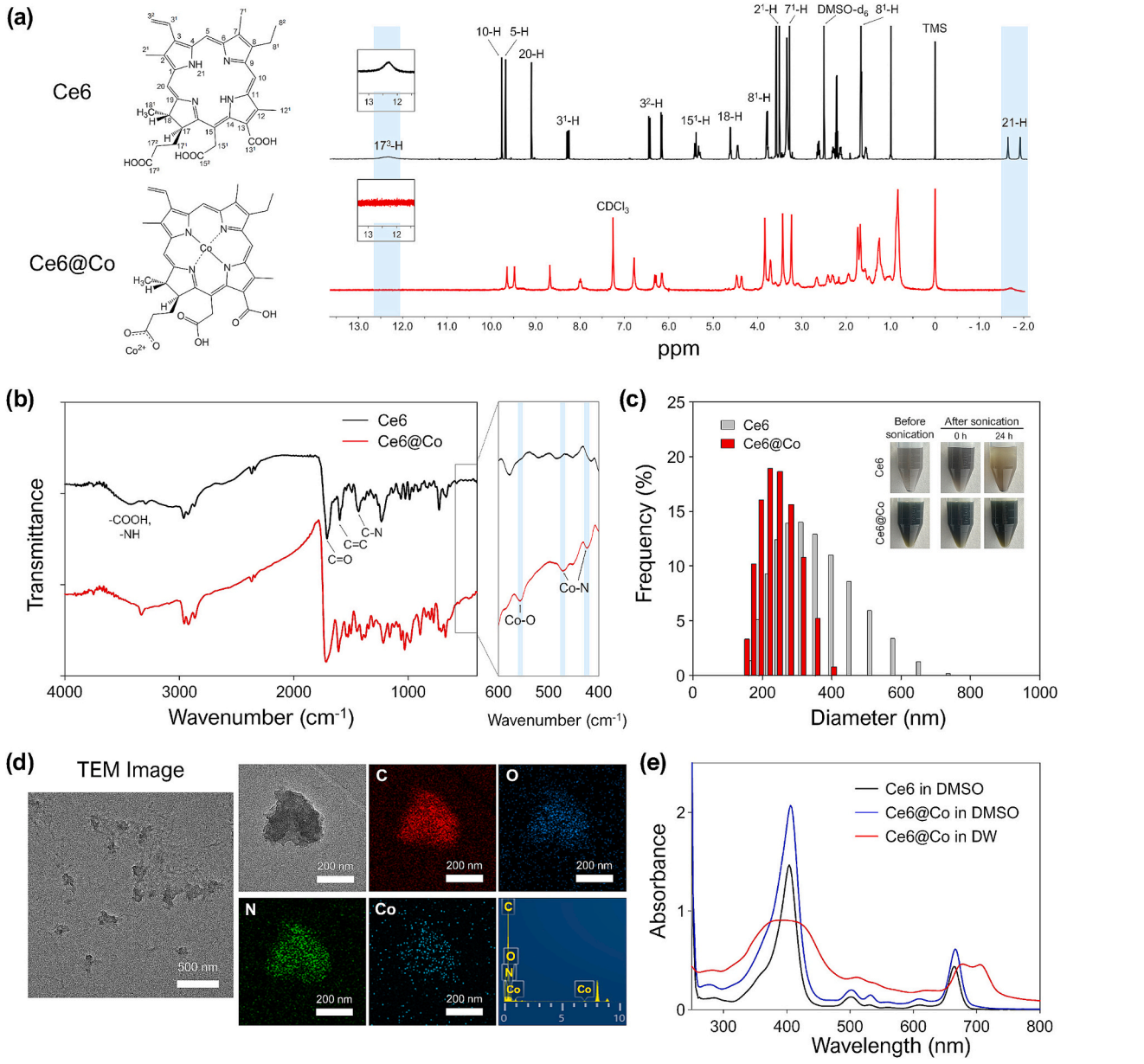


**Fig. 1.** Ce6@Co nanoparticle characterization. (a) $^{1}$H NMR and (b) Free Ce6 and Ce6@Co nanoparticle FT-IR spectra. (c) Particle size distributions of free Ce6 and Ce6@Co nanoparticles. Inset: Photos of free Ce6 and Ce6@Co nanoparticle solutions in DW before and after sonication. (d) TEM image, elemental mapping of C, O, N, and Co, and EDS spectrum of Ce6@Co nanoparticles. (e) UV/Vis spectra of Ce6 in DMSO and Ce6@Co nanoparticles in DMSO or DW.

et al., 2023; Song et al., 2011). This metal ion coordination helps construct nanostructures that enhance Ce6's aqueous solubility and colloidal stability by mitigating hydrophobic aggregation. Concurrently, among transition metal ions, $Co^{2+}$ exhibits high catalytic activity in Fenton-like reactions, efficiently decomposing $H_2O_2$ to ·OH for CDT (Liu et al., 2017b; Park et al., 2023; Song et al., 2024; Zhang et al., 2019). Based on these principles, we synthesized $Co^{2+}$-coordinated Ce6 (Ce6@Co) nanoparticles to combine Ce6's photodynamic activity (PDT) with $Co^{2+}$-driven ·OH generation (CDT). This dual-modal therapeutic approach addresses hydrophobic aggregation while enhancing therapeutic efficacy via cytotoxic ROS production.

The Ce6 and $Co^{2+}$ concentrations in Ce6@Co nanoparticles were determined using UV/Vis spectroscopy and ICP analysis. Based on the Ce6 standard curve (Fig. S1), UV/Vis spectroscopy indicated a Ce6 concentration of 0.87 mg/mL (1461.3 μM) in the nanoparticle solution. ICP analysis confirmed a $Co^{2+}$ concentration of 0.0031 mg/mL (56 μM). To confirm Ce6@Co nanoparticle synthesis, $^{1}$H NMR and FT-IR analyses were performed. The $^{1}$H NMR spectra (Fig. 1a) revealed that Ce6@Co retained the characteristic peaks of free Ce6 in the 0 to 10 ppm range. However, free Ce6 exhibited two sharp inner N—H proton peaks at −1.65 and − 1.9 ppm (arising from the porphyrin macrocycle) and a broad carboxyl (-COOH) proton peak at 12.3 ppm ($17^{3}$-C position). These peaks disappeared in the Ce6@Co group, likely owing to $Co^{2+}$ coordination with the macrocycle's nitrogen atoms and Ce6's carboxyl groups (Gjuroski et al., 2021; Hasobe et al., 2010; Isakau et al., 2007; Pandit et al., 2024). Ce6@Co FT-IR spectra revealed further structural evidence for $Co^{2+}$ coordination (Fig. 1b). Although the 1000 to 1750 $cm^{-1}$ range retained free Ce6's characteristic stretching modes (e.g., C═O at ~1708 $cm^{-1}$, C═C at 1560 $cm^{-1}$, and C—N at 1480 $cm^{-1}$), new vibration bands emerged at 468 $cm^{-1}$ and 424 $cm^{-1}$, assigned to Co—N stretching modes from $Co^{2+}$ binding to pyrrolic nitrogen atoms within Ce6's porphyrin macrocycle. A distinct peak at 557 $cm^{-1}$ corresponded to Co—O stretching, indicative of carboxylate coordination to $Co^{2+}$ (Chaudhary and Mishra, 2017; Rubab et al., 2022). Attenuation of the

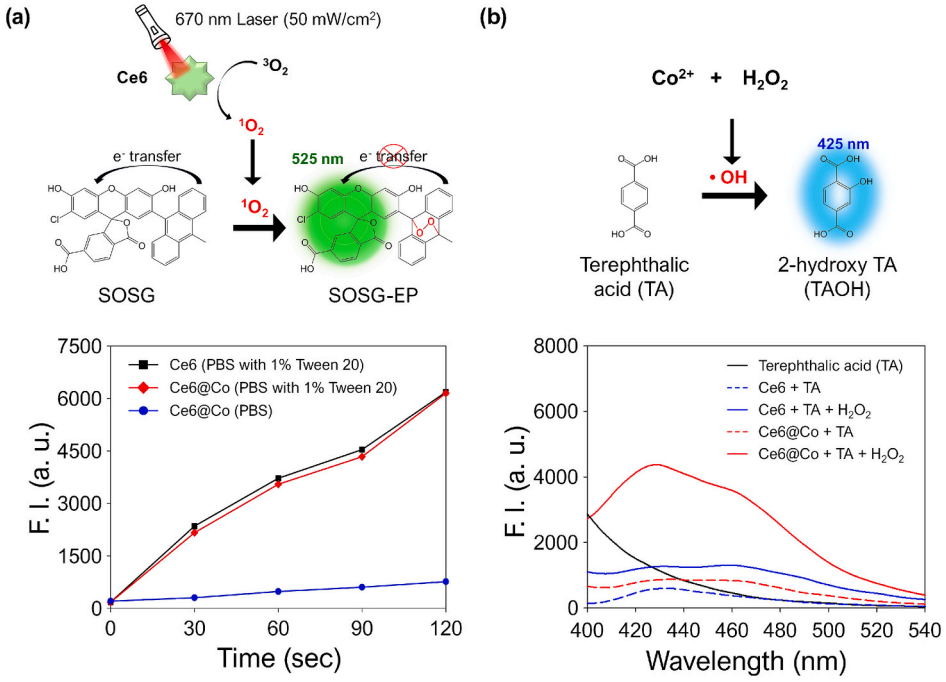


**Fig. 2.** Dual-ROS generation properties of Ce6@Co nanoparticles for singlet oxygen ($^1O_2$) generation under laser irradiation (670 nm, 50 mW/cm$^2$) and hydroxyl radical (·OH) production via $Co^{2+}$-catalyzed Fenton-like reactions. (a) $^1O_2$ generation via free Ce6 (PBS with 1 % Tween 20), Ce6@Co (PBS with 1 % Tween 20), and Ce6@Co (PBS without surfactant). SOSG is highly selective for singlet oxygen forming an endoperoxide anthracene upon reaction, which is no longer an efficient intramolecular electron donor, leading to fluorescence emission at 525 nm. (b) ·OH production was assessed under various conditions: TA only, Ce6 + TA, Ce6 + TA + 500 μM $H_2O_2$, Ce6@Co + TA, and Ce6@Co + TA + 500 μM $H_2O_2$. TA acts as a ·OH fluorescence probe, forming fluorescent 2-hydroxy terephthalic acid (TAOH) upon reaction with ·OH, which emits at 425 nm.

broad band at 3300–3500 cm$^{-1}$ (attributed to –NH and –COOH groups in free Ce6) in Ce6@Co suggests deprotonation of the macrocycle's inner N—H and carboxyl moieties upon $Co^{2+}$ chelation (Gjuroski et al., 2021; Hasobe et al., 2010).

The particle size distribution, colloidal and storage stability, and zeta potential of Ce6 and Ce6@Co nanoparticles were evaluated using DLS and photographic analysis. Free Ce6 nanoparticles, prepared without $Co^{2+}$, exhibited a hydrodynamic mean size of 317.8 ± 101.6 nm, *Z*-average size of 608.8 nm, and PDI of 0.341, indicating a broad size distribution. In contrast, Ce6@Co nanoparticles displayed a smaller hydrodynamic mean size of 227.3 ± 51.5 nm, Z-average size of 230.4 nm, and lower PDI of 0.207, reflecting a narrower and more uniform size distribution. As shown in the inset of Fig. 1c, free Ce6 nanoparticles aggregated and precipitated even after sonication, while Ce6@Co nanoparticles remained well-dispersed in DW for 24 h post-sonication. Consistently, Z-average sizes of free Ce6 nanoparticles greatly increased and fluctuated during long-term storage in DW, pH 7.4 PBS, and 10 % FBS at 4 °C (Fig. S2a), whereas Ce6@Co nanoparticle sizes remained stable under the same conditions (Fig. S2b). The zeta potential of Ce6@Co nanoparticles was −42.7 mV, slightly less negative than the −46.5 mV for free Ce6 nanoparticles (Fig. S3), likely owing to $Co^{2+}$ coordination with Ce6, reducing surface charge. These findings suggested that incorporating $Co^{2+}$ during nanoparticle synthesis enhances colloidal stability and yields more homogenous particle sizes.

Forming Ce6@Co nanoparticles by incorporating $Co^{2+}$ with Ce6 during synthesis was confirmed by TEM and UV/Vis spectroscopy. TEM showed near-spherical Ce6@Co nanoparticles sizes ranging from 200 to 250 nm (Fig. 1d), consistent with DLS measurements. Elemental mapping via EDS demonstrated carbon, oxygen, nitrogen, and cobalt within the nanoparticles (Fig. 1d), verifying successful coordination of $Co^{2+}$ with Ce6. In the UV/Vis spectra, both free Ce6 and Ce6@Co nanoparticles in DMSO exhibited a strong Soret band at 405 nm and Q-bands ranging from 480 to 700 nm, characteristic of Ce6's optical properties (Fig. 1e). However, when Ce6@Co nanoparticles were dispersed in DW, these peaks became broader and less intense, attributed to light transmittance interference in aqueous environments (Ahn et al., 2020). Notably, compared to Ce6 in DMSO, Ce6@Co nanoparticles in DW showed a broadened Soret band and a red-shifted Q-band, with four distinct Q-band peaks indicating coordination interactions between $Co^{2+}$ ions and Ce6's carboxyl groups (Pei et al., 2023). Upon solubilizing Ce6@Co nanoparticles in DMSO, disrupting nanoparticle structure, the Soret band narrowed and part of the Q-band shifted back to blue, suggesting the J-aggregate formation of Ce6 molecules within nanoparticles (Qu et al., 2023). This J-type aggregation is likely due to spatial interactions of transition dipole moments and π-π stacking among Ce6 molecules during nanoparticle synthesis (Ocakoglu et al., 2014; Pei et al., 2023), a phenomenon also observed in other photosensitizer-based nanomaterials (Demberelnyamba et al., 2008; Zou et al., 2020).

### 3.2. Cytotoxic dual-ROS generating ability of Ce6@Co nanoparticles

In this study, Ce6@Co nanoparticles were synthesized to integrate Ce6's PDT capability with $Co^{2+}$-mediated ·OH generation (CDT) for enhanced therapeutic efficacy. $^1O_2$ generation was measured using the SOSG assay to evaluate phototherapeutic potential of Ce6@Co nanoparticles (Fig. 2a). Free Ce6 nanoparticles exhibited fluorescence dequenching when solubilized in pH 7.4 PBS containing 1 % Tween 20 (a surfactant that mimics the cytosolic environment by disrupting the dense nanoparticle structure) (Fig. S4) (Park et al., 2020). Subsequent laser irradiation increased time-dependent $^1O_2$ generation. In contrast, Ce6@Co nanoparticles in pH 7.4 PBS without surfactant exhibited negligible fluorescence emission (a quenched state, Fig. S4), and thus they showed only a slow increase in $^1O_2$ production, indicating low-phototoxic state. However, when Ce6@Co nanoparticles were dequenched in pH 7.4 PBS with surfactant (Fig. S4), $^1O_2$ generation rapidly increased match free Ce6 levels, demonstrating the phototoxic activity of Ce6@Co is restored in a cytosol-mimicking environment. These results indicate that Ce6@Co nanoparticles remain

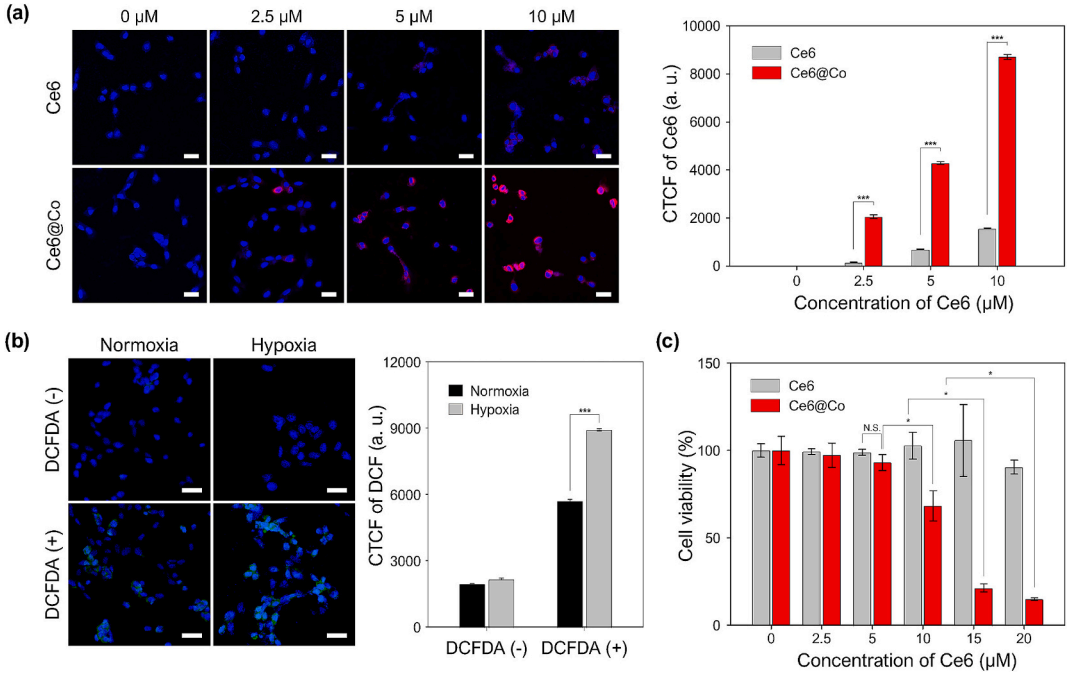


**Fig. 3.** Intracellular uptake, intracellular $H_2O_2$ levels under normoxia and hypoxia, and dark toxicity. (a) Confocal images and quantitative analysis of free Ce6 and Ce6@Co nanoparticle intracellular uptake in SCC7 cells. Scale bar: 30 μm, ***$p < 0.005$. (b) Confocal images and quantitative analysis of intracellular $H_2O_2$ levels of SCC7 cells under normoxia and hypoxia. Scale bar: 30 μm. ***p < 0.005. (c) Cell viabilities of SCC7 cells treated with free Ce6 or Ce6@Co nanoparticles at various concentrations (0, 2.5, 5, 10, 15, and 20 μM of Ce6) under dark conditions. *$p < 0.05$. N.S. = No significance.

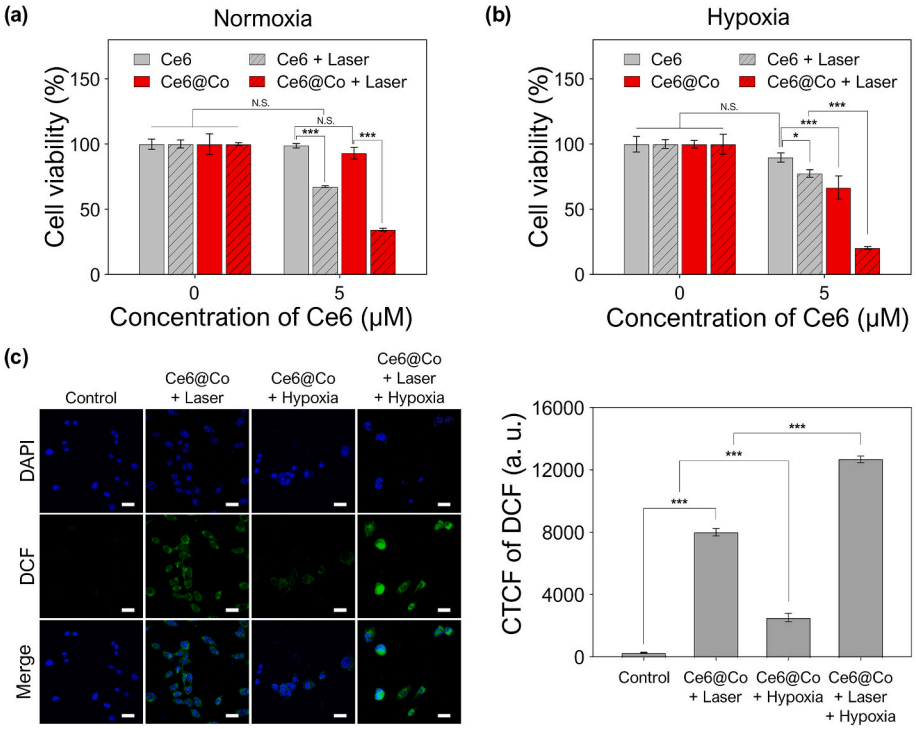


**Fig. 4.** In vitro therapeutic effects and ROS amplification of Ce6@Co nanoparticles on SCC7 cells. (a and b) Cell viabilities of SCC7 cells treated with free Ce6 (5 μM) or Ce6@Co nanoparticles (equivalent 5 μM of Ce6) under (a) normoxic and (b) hypoxic conditions with or without 670 nm laser irradiation (50 mW/cm$^2$) for 30 s. *p < 0.05, ***p < 0.005. N.S. = No significance. (c) CLSM images and quantitative analysis comparing intracellular ROS generation in SCC7 cells under the following conditions: Ce6@Co nanoparticles with irradiation under normoxia, Ce6@Co nanoparticles without irradiation under hypoxia, or Ce6@Co nanoparticles with irradiation under hypoxia. Scale bar: 30 μm. ***p < 0.005.

photodynamically inactive in their aggregated, quenched state, and regain strong phototherapeutic activity upon dequenching (Park et al., 2020; Song et al., 2021), indicating their phototherapeutic potential.

To assess the chemodynamic potential of Ce6@Co nanoparticles, $Co^{2+}$-mediated ·OH production was further evaluated using TA as a fluorescence probe, forming fluorescent 2-hydroxy terephthalic acid

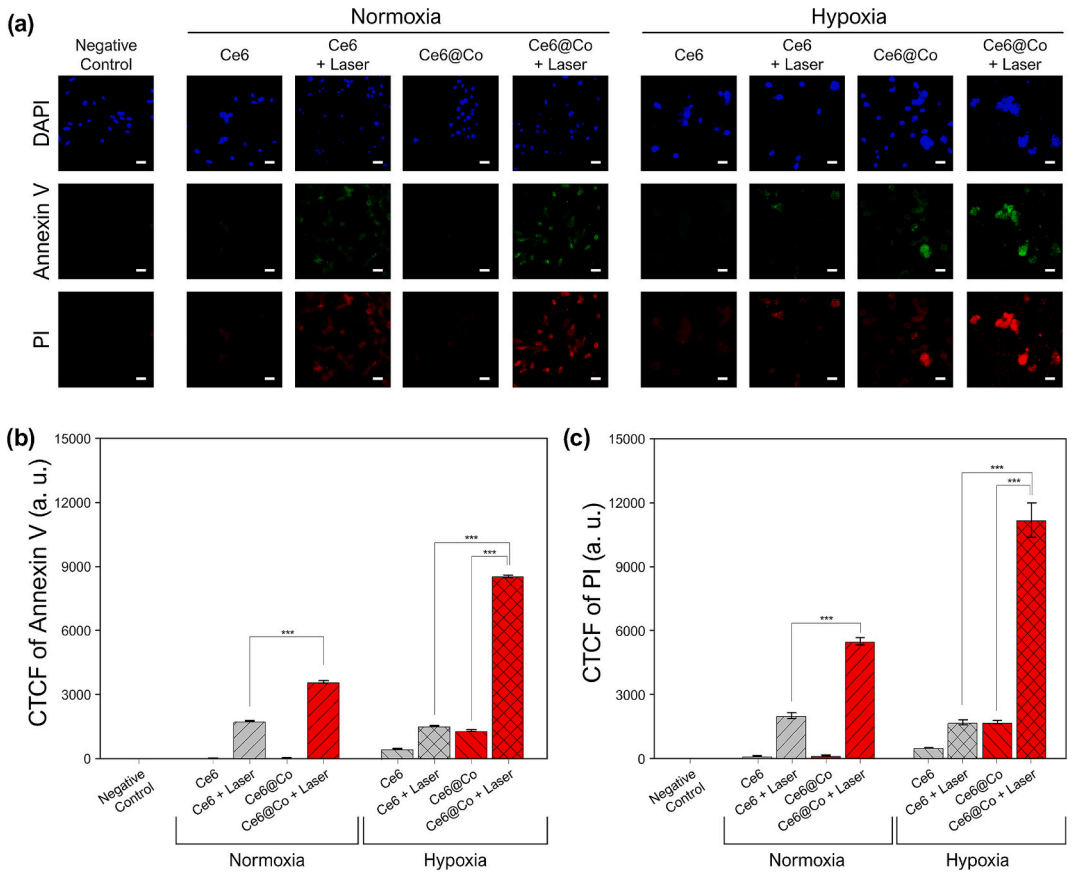


**Fig. 5.** In vitro apoptosis assay. (a) CLSM images for Annexin V (green) and PI (red)-stained SCC7 cells treated with free Ce6 (5 μM) or Ce6@Co nanoparticles (equivalent 5 μM of Ce6) under normoxic and hypoxic conditions with or without 670 nm laser irradiation (50 mW/cm$^2$) for 30 s. Scale bar: 30 μm. Quantitative analysis of (b) Annexin V and (c) PI fluorescence intensities in each group. ***$p < 0.005$. (For interpretation of the references to colour in this figure legend, the reader is referred to the web version of this article.)

(TAOH) upon reaction with ·OH (Liu et al., 2017a). TA alone, or in combination with Ce6 or Ce6@Co (without $H_2O_2$), and TA with Ce6 under $H_2O_2$, showed no fluorescence at 425 nm (Fig. 2b). In contrast, TA with Ce6@Co under $H_2O_2$ exhibited a significant and time-dependent increase in fluorescence intensity at 425 nm (Fig. 2b and Fig. S5), indicating efficient $Co^{2+}$-mediated ·OH generation via Fenton-like reactions. These findings confirmed that Ce6@Co nanoparticles possess both activatable photodynamic and chemodynamic therapeutic potential for synergistic cancer therapy.

### 3.3. *In vitro cellular uptake, intracellular ROS levels in normoxia and hypoxia, and dark toxicity*

The intracellular uptake of Ce6@Co nanoparticles was assessed using CLSM, and fluorescence intensities were quantified (Fig. 3a). We selected 24 h as the optimal timepoint for cellular uptake analysis because both free Ce6 and Ce6@Co nanoparticles exhibited maximal fluorescence intensity at this interval, as demonstrated in Fig. S6. Cellular uptake of Ce6@Co nanoparticles was significantly higher compared to that of free Ce6 at all tested concentrations in SCC7 cells. Nanoparticle size critically influences cellular uptake and intracellular distribution (Augustine et al., 2020). DLS measurements (Fig. 1c) confirmed the smaller and more uniform size of Ce6@Co nanoparticles enhances cellular internalization efficiency via endocytosis or passive diffusion, compared to free Ce6. Their superior aqueous dispersibility attributed to stable colloidal formulation also contributed to improved uptake (Jeong et al., 2011; Jo et al., 2023).

Intracellular ROS levels were assessed in SCC7 cells under normoxic and hypoxic conditions using the DCFDA. Under normoxia, DCFDA is hydrolyzed by cellular esterases into non-fluorescent 2′,7′-dichlorodihydrofluorescein (DCFH). In hypoxic conditions, elevated ROS (including $H_2O_2$) oxidizes DCFH into strongly fluorescent 2′,7′-dichlorofluorescein (DCF), enabling ROS detection (Kim et al., 2010). CLSM images revealed a moderate increase in fluorescence intensity in normoxic SCC7 cells treated with DCFDA compared to untreated controls (Fig. 3b). Under hypoxia, fluorescence intensity increased 1.56-fold, consistent with a previous study demonstrating that hypoxia amplifies $H_2O_2$ generation (Kim et al., 2023).

The in vitro dark toxicity of free Ce6 and Ce6@Co nanoparticles was evaluated using a CCK-8 assay (Fig. 3c). Free Ce6 treatment showed a > 95 % cell viability at all tested concentrations (2.5–20 μM), indicating no significant cellular toxicity. In contrast, Ce6@Co nanoparticles exhibited concentration-dependent cytotoxicity, with a notable reduction in cell viability observed at concentrations ≥10 μM. This cytotoxic effect is attributed to ·OH production via $Co^{2+}$-mediated Fenton-like reactions, a mechanism consistent with a previous study demonstrating metal ion-driven ROS generation in tumor microenvironments (Tian et al., 2022), triggered via endogenous $H_2O_2$ levels in normoxic tumor cells (Fig. 3b). However, they exhibited no significant cytotoxicity in normal HDF cells (Fig. S7), which contain significantly lower endogenous $H_2O_2$ levels than cancer cells. This selective safety originates from $H_2O_2$-dependent $Co^{2+}$-mediated Fenton-like reactions required for cytotoxic ·OH generation. As revealed by TA assays (Figs. 2b and S5), insufficient $H_2O_2$ in normal cells prevents catalytic ·OH production. These findings confirm that Ce6@Co nanoparticles remain biologically safe in healthy cells. Collectively, these results established 5 μM Ce6 as the threshold concentration under dark conditions, as no cytotoxicity was observed at this level. Consequently, subsequent experiments used 5 μM Ce6 to

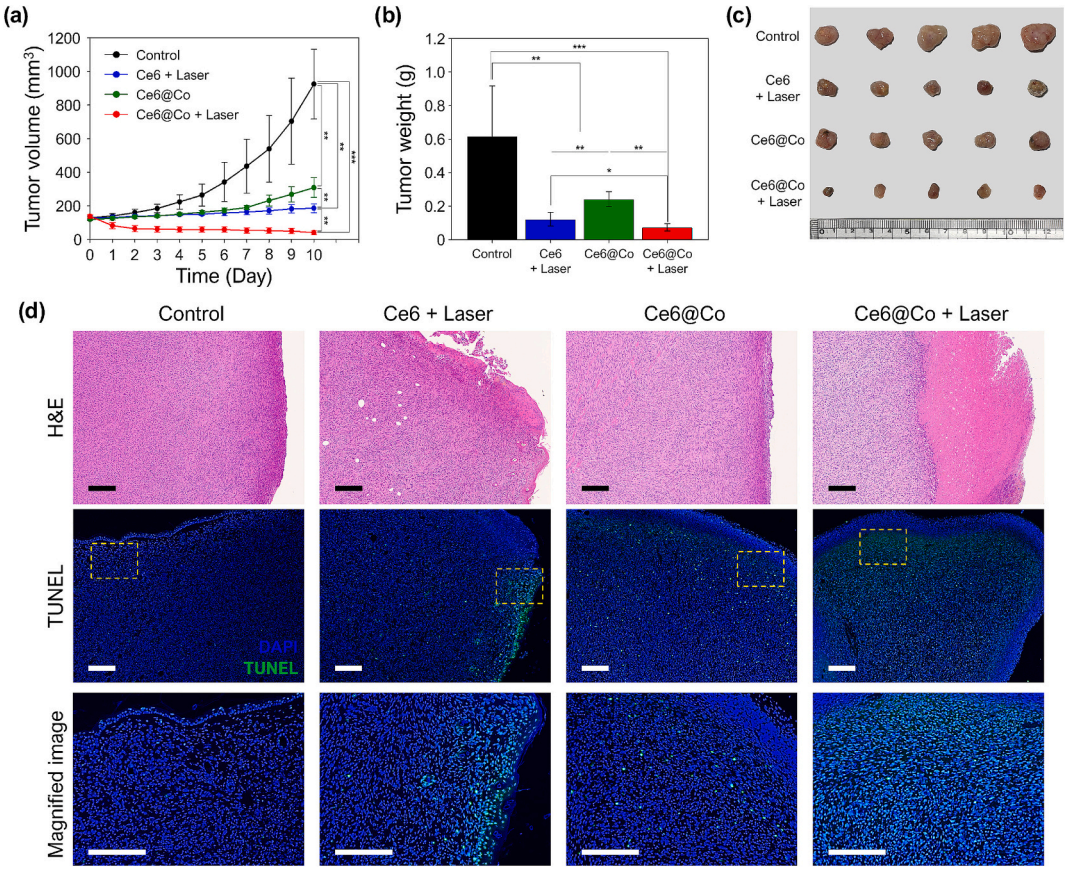


**Fig. 6.** In vivo therapeutic effects of Ce6@Co nanoparticles on SCC7-tumor-bearing mice. (a) Tumor volumes of SCC7-tumor-bearing mice after PBS (control), free Ce6 (1 mg/kg) + laser irradiation, Ce6@Co nanoparticles (an equivalent Ce6 dose of 1 mg/kg), or Ce6@Co nanoparticles (an equivalent Ce6 dose of 1 mg/kg) + laser irradiation treatments. Free Ce6 and Ce6@Co nanoparticles were administered via intratumoral injection. In the two groups designated for PDT, tumors were irradiated with a 670 nm laser at 100 mW/cm$^2$ for 20 min, 6 h post-injection. $^{**}p < 0.01$, $^{***}p < 0.005$. (b) Tumor weight and (c) photographs of excised tumors from each treatment group at the end of the experiment. Scale bar: 1 cm. $^{*}p < 0.05$, $^{**}p < 0.01$, $^{***}p < 0.005$. (d) Representative images of tumor tissue H&E and TUNEL staining. Nuclei are stained blue (DAPI), and apoptotic cells are stained green (TUNEL). Scale bars: 200 μm. (For interpretation of the references to colour in this figure legend, the reader is referred to the web version of this article.)

assess antitumor efficacy while minimizing nonspecific toxicity.

### 3.4. *In vitro anticancer effects of Ce6@Co nanoparticles*

The in vitro therapeutic efficacy of Ce6@Co nanoparticles was investigated in SCC7 cells under normoxic and hypoxic conditions. Untreated control groups and cells treated with free Ce6 without laser irradiation exhibited negligible cytotoxicity under both conditions (Fig. 4a and b). Under normoxia, laser irradiation (670 nm) of free Ce6 reduced cell viability to 67.3 %, demonstrating PDT efficacy mediated via $^1O_2$ generation. In contrast, under hypoxia, free Ce6 with laser irradiation resulted in a 77.4 % viability, reflecting diminished PDT efficiency owing to oxygen scarcity limiting $^1O_2$ production (Cen et al., 2023). In comparison, Ce6@Co nanoparticles under identical conditions (670 nm laser irradiation under normoxia) lowered viability to 34.4 %, demonstrating enhanced therapeutic efficacy due to improved cellular uptake (attributed to their stable colloidal formulation, Fig. 3a) and dual ROS production ($^1O_2$ from photodynamic activation and ·OH via $Co^{2+}$-mediated Fenton-like reactions, Fig. 4c). Under hypoxia, Ce6@Co nanoparticles without laser irradiation induced 66.7 % cytotoxicity (33.3 % viability), via $Co^{2+}$-catalyzed hypoxia-elevated $H_2O_2$ decomposition into ·OH, bypassing oxygen dependency. This aligns with a previous study reporting hypoxia-induced $H_2O_2$ accumulation in tumors, potentiating metal ion-driven ROS generation (Tian et al., 2022). Combining Ce6@Co nanoparticles with laser irradiation under hypoxia further reduced viability to 20.48 %, highlighting synergistic ROS amplification ($^1O_2$ + ·OH, Fig. 4c). This combined efficacy surpassed normoxic PDT outcomes (34.4 % viability), highlighting CDT's potential to compensate for PDT's oxygen dependency in hypoxic tumor microenvironments.

To further evaluate the in vitro combined therapeutic effects of Ce6@Co nanoparticles, apoptotic cell death in SCC7 cells was assessed via Annexin V-PI staining and CLSM under normoxic and hypoxic conditions (Fig. 5). Under both conditions, untreated controls and free Ce6-treated cells without irradiation exhibited negligible Annexin V/PI fluorescence (Figs. 5a-c), confirming minimal baseline apoptosis. Laser irradiation (670 nm) of free Ce6 under normoxia and hypoxia induced moderate apoptosis signals, reflecting oxygen-dependent photodynamic activity mediated by $^1O_2$ generation. In contrast, Ce6@Co nanoparticles under normoxia with irradiation produced significantly stronger Annexin V/PI fluorescence, attributed to enhanced cellular uptake and dual ROS production mediated by photodynamic ($^1O_2$) and chemodynamic (·OH) activation. Under hypoxia, Ce6@Co nanoparticles without irradiation induced moderate apoptosis, driven by hypoxia-elevated $H_2O_2$ levels fueling $Co^{2+}$-mediated ·OH generation via Fenton-like reactions. The strongest apoptotic response was observed when Ce6@Co nanoparticles were combined with laser irradiation under hypoxia (Figs. 5a-c), highlighting the synergistic ROS amplification via integrated PDT and CDT. These results demonstrated that Ce6@Co nanoparticles effectively overcome hypoxia-associated limitations in conventional PDT by leveraging dual oxygen-dependent (PDT) and oxygen-independent (CDT) mechanisms.

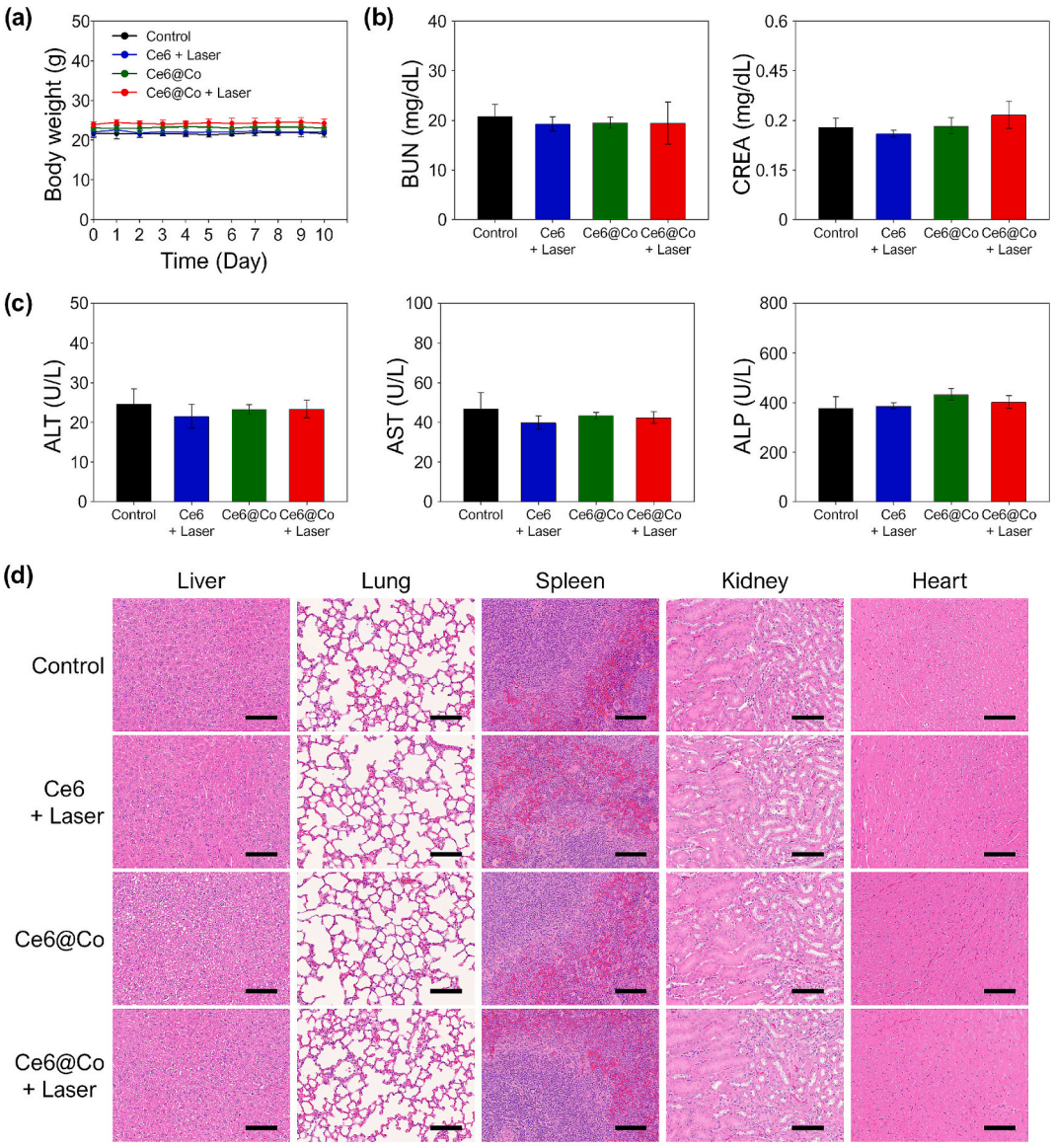


**Fig. 7.** In vivo biosafety study. (a) Body weight changes of SCC7 tumor-bearing mice in each group after PBS (control), free Ce6 (1 mg/kg) + laser irradiation, Ce6@Co nanoparticles (an equivalent Ce6 dose of 1 mg/kg), or Ce6@Co nanoparticles (an equivalent Ce6 dose of 1 mg/kg) + laser irradiation treatments. (b and c) Serum biochemistry analysis of mice after treatment. (b) BUN and CREA for renal function, and (c) ALT, AST, and ALP for hepatic function. (d) H&E staining of major organs (liver, lung, spleen, kidney, and heart) from each treatment group, indicating no observable organ damage. Scale bars: 100 μm.

### *3.5. In vivo therapeutic effects of Ce6@Co nanoparticles on SCC7 tumor-bearing mice*

The in vivo therapeutic efficacy of Ce6@Co nanoparticles was evaluated using the SCC7 solid tumor model, where mice bearing tumors of 100–150 $mm^3$ were administered intratumoral PBS, free Ce6 (1 mg/kg), or Ce6@Co nanoparticles (1 mg Ce6/kg) injections. Intratumoral delivery was strategically used to maximize Ce6 retention at the tumor site, minimize phototoxicity to surrounding healthy tissues, and overcome the rapid systemic clearance typically associated with intravenous administration (Jeong et al., 2011; Ma et al., 2021b). Tumor volumes were monitored daily for 10 d (Fig. 6a), and tumor weight was measured at the endpoint (Fig. 6b) to assess therapeutic outcomes. The control group exhibited rapid tumor progression, whereas Ce6@Co nanoparticles without irradiation demonstrated enhanced antitumor efficacy attributed to their superior aqueous dispersibility and optimized nanoparticle size, facilitating more uniform intratumoral distribution and greater retention (Fig. S8), thereby achieving effective CDT. Although free Ce6 exhibited less homogenous tumor distribution than Ce6@Co nanoparticles (Fig. S8), it could achieve increased antitumor effects under laser irradiation owing to its photodynamic activity. Notably, the Ce6@Co nanoparticles combined with laser irradiation group showed the most significant tumor growth inhibition, with complete suppression observed and the smallest tumor volumes and weight (Fig. 6a–c). These results confirmed the robust antitumor effects of Ce6@Co nanoparticles, particularly when combined with laser irradiation, via synergistic PDT and CDT activation, supported by their favorable intratumoral distribution and retention.

The in vivo antitumor effects of Ce6@Co nanoparticles combined with laser irradiation were further evaluated on day 10 using H&E and TUNEL staining of tumor (Fig. 6d). H&E staining of the control group revealed normal tumor morphology with abundant viable cells and no signs of necrosis or apoptosis. Tumors treated with Ce6@Co nanoparticles alone had predominantly viable cells; however, they exhibited weak apoptotic signals, likely from chemodynamic activity within the tumor microenvironment. In contrast, both free Ce6 plus laser

irradiation and Ce6@Co nanoparticles plus laser irradiation groups showed visible scab formation and increased apoptosis, confirmed by H&E and TUNEL staining. Notably, the Ce6@Co nanoparticles plus laser irradiation group demonstrated more pronounced tumor tissue damage, including nuclear condensation, cytoplasmic shrinkage, and loss of structural integrity than the free Ce6 plus laser irradiation group. TUNEL analysis revealed a significantly larger area of TUNEL-positive staining in the Ce6@Co nanoparticles plus laser irradiation group, indicating substantial DNA fragmentation and apoptosis. The widespread distribution of TUNEL-positive fluorescence throughout the tumor sections in this group is attributed to the favorable intratumoral distribution and retention of Ce6@Co nanoparticles, enhancing antitumor efficacy via synergistic PDT and CDT activation.

### 3.6. *In vivo biosafety assay*

The in vivo biosafety of nanomaterials is crucial for their biomedical application, as their unique physicochemical properties influence toxicity, biodistribution, and tissue compatibility (Awashra and Mlynarz, 2023). To evaluate the biosafety, SCC7 tumor-bearing mice were assigned to control, free Ce6 with irradiation, Ce6@Co nanoparticles alone, and Ce6@Co nanoparticles with irradiation groups. Systemic toxicity was assessed by monitoring body weight, an established criterion that considers a $\geq$ 20 % reduction in body weight as a sign of in vivo toxicity (Van Berlo et al., 2022). As shown in Fig. 7a, no significant changes in body weight of mice were observed among the groups, indicating no acute toxicity. Serum biochemical analyses, including measurements of BUN, CREA, ALT, AST, and ALP, revealed no substantial differences between groups (Fig. 7b and c), suggesting preserved hepatic and renal function. Furthermore, histological examination of major organs (e.g., liver, lung, spleen, kidney, and heart) via H&E staining showed no pathological abnormalities in any group (Fig. 7d). Collectively, these results demonstrated that both free Ce6 and Ce6@Co nanoparticles, even when combined with laser irradiation, exhibit high biocompatibility and do not induce significant systemic toxicity following intratumoral administration, supporting their potential for safe in vivo application.

While Ce6@Co nanoparticles have demonstrated excellent therapeutic efficacy and biosafety in preclinical models, several important challenges must be addressed to enable successful clinical translation. First, the coordination-driven synthesis process requires further optimization to ensure scalable and reproducible production with consistent physicochemical properties. Comprehensive long-term biocompatibility and chronic toxicity studies are also essential, particularly due to the involvement of transition metal ions, to evaluate potential accumulation and organ-specific effects. Additionally, detailed investigations into pharmacokinetics, biodegradation, and clearance pathways are necessary to satisfy regulatory requirements. The development of GMP-compliant manufacturing protocols and robust quality control systems will be critical to ensure product safety and uniformity. Addressing these key considerations will further strengthen the translational potential of this dual-modal nanoplatform for clinical cancer therapy.

## 4. Conclusion

This study demonstrates that Ce6@Co nanoparticles, synthesized by coordinating $Co^{2+}$ with Ce6, effectively integrate PDT and CDT to achieve potent antitumor effects in solid tumors. The nanoparticles self-assembled uniformly with an average diameter of approximately 230 nm and improved aqueous dispersibility and colloidal stability compared to free Ce6. This dual-modality approach leverages the photosensitizing properties of Ce6 to generate $^1O_2$ under laser irradiation, whereas coordinated $Co^{2+}$ ions catalyze Fenton-like reactions to produce cytotoxic ·OH in the hypoxic tumor microenvironment. Such synergistic action enhances ROS production, leading to robust tumor cell apoptosis and marked tumor growth inhibition. In vitro studies revealed that Ce6@Co nanoparticles displayed enhanced cellular uptake and induced significant apoptosis via amplified ROS generation, even under hypoxia conditions with laser irradiation. In vivo, intratumoral injection of Ce6@Co nanoparticles with laser irradiation achieved complete tumor suppression, attributed to favorable tumor retention and synergistic effects of PDT and CDT. Notably, no systemic toxicity was observed, as indicated by stable body weight, normal serum biochemical parameters, and unchanged major organs histology. Integrating PDT with metal ion-mediated CDT addresses the oxygen-dependent limitations of traditional photodynamic monotherapy. Overall, Ce6@Co nanoparticles represent a promising hypoxia-adaptive nanoplatform, integrating oxygen-independent CDT with activatable PDT for the safe and effective treatment of solid tumors, particularly hypoxic solid tumors.

## CRediT authorship contribution statement

**Yeji Chang:** Writing – original draft, Methodology, Investigation, Funding acquisition, Formal analysis, Conceptualization. **Yong Geun Lim:** Investigation, Formal analysis. **Kyeongsoon Park:** Writing – review & editing, Supervision, Funding acquisition, Conceptualization.

## Declaration of competing interest

The authors declare that they have no known competing financial interests or personal relationships that could have appeared to influence the work reported in this paper.

## Acknowledgements

This research was supported by grants from the National Research Foundation of Korea (NRF-2023R1A2C1004940) and Basic Science Research Program through the National Research Foundation of Korea (NRF) funded by the Ministry of Education (RS-2024-00462761). Y.J. Chang was supported by the Chung-Ang University Graduate Research Scholarship in 2023. The authors thank the BT research facility center of Chung-Ang University.

## Appendix A. Supplementary data

Supplementary data to this article can be found online at https://doi.org/10.1016/j.ijpx.2025.100348.

## Data availability

Data will be made available on request.

## References

Abrahamse, H., Hamblin, M.R., 2016. New photosensitizers for photodynamic therapy. Biochem. J. 473, 347–364.
Ahn, J.W., Kim, J.H., Park, K., 2020. In vitro photodynamic effects of the inclusion nanocomplexes of glucan and chlorin e6 on atherogenic foam cells. Int. J. Mol. Sci. 22, 177.
Alsaab, H.O., Alghamdi, M.S., Alotaibi, A.S., Alzhrani, R., Alwuthaynani, F., Althobaiti, Y.S., Almalki, A.H., Sau, S., Iyer, A.K., 2020. Progress in clinical trials of photodynamic therapy for solid tumors and the role of nanomedicine. Cancers (Basel) 12, 2793.
An, J., Tang, S., Hong, G., Chen, W., Chen, M., Song, J., Li, Z., Peng, X., Song, F., Zheng, W.H., 2022. An unexpected strategy to alleviate hypoxia limitation of photodynamic therapy by biotinylation of photosensitizers. Nat. Commun. 13, 2225.
Augustine, R., Hasan, A., Primavera, R., Wilson, R.J., Thakor, A.S., Kevadiya, B.D., 2020. Cellular uptake and retention of nanoparticles: insights on particle properties and interaction with cellular components. Mater Today Commun 25, 101692.
Awashra, M., Mlynarz, P., 2023. The toxicity of nanoparticles and their interaction with cells: an in vitro metabolomic perspective. Nanoscale Adv 5, 2674–2723.
Badiee, P., Maritz, M.F., Dmochowska, N., Cheah, E., Thierry, B.J.A.A.M., 2022. Intratumoral anti-PD-1 nanoformulation improves its biodistribution. ACS Appl. Mater. Interfaces 14, 15881–15893.

Balem, F., Yanamala, N., Klein-Seetharaman, J., 2009. Additive effects of chlorin e6 and metal ion binding on the thermal stability of rhodopsin in vitro. Photochem. Photobiol. 85, 471–478.
Cen, Y., Chen, X., Liu, Y., Yu, B., Yan, M., Yang, N., Kong, R., Li, S., Ti, H., Cheng, H., 2023. Drug induced mitochondria dysfunction to enhance photodynamic therapy of hypoxic tumors. J. Control. Release 358, 654–666.
Chai, T., Li, Y.Y., Kenar, N., Lim, H.S., Temple, H., Chen, X.Y., Chen, W., 2023. Some synergetic therapy strategies for overcoming hypoxia for photodynamic therapy of cancer. J Cancer Metas Treat 9. N/A-N/A.
Chaudhary, N.K., Mishra, P., 2017. Metal complexes of a novel schiff base based on penicillin: characterization, molecular modeling, and antibacterial activity study. Bioinorg. Chem. Appl. 2017, 6927675.
Cheng, D.B., Zhang, X.H., Gao, Y.J., Ji, L., Hou, D., Wang, Z., Xu, W., Qiao, Z.Y., Wang, H., 2019. Endogenous reactive oxygen species-triggered morphology transformation for enhanced cooperative interaction with mitochondria. J. Am. Chem. Soc. 141, 7235–7239.
Correia, J.H., Rodrigues, J.A., Pimenta, S., Dong, T., Yang, Z., 2021. Photodynamic therapy review: principles, photosensitizers, applications, and future directions. Pharmaceutics 13, 1332.
Demberelnyamba, D., Ariunaa, M., Shim, Y.K., 2008. Newly synthesized water soluble cholinium-purpurin photosensitizers and their stabilized gold nanoparticles as promising anticancer agents. Int. J. Mol. Sci. 9, 864–871.
Escudero, A., Carrillo-Carrión, C., Castillejos, M.C., Romero-Ben, E., Rosales-Barrios, C., Khiar, N., 2021. Photodynamic therapy: photosensitizers and nanostructures. Mater Chem Front 5, 3788–3812.
Gjuroski, I., Furrer, J., Vermathen, M., 2021. Probing the Interactions of porphyrins with macromolecules using NMR spectroscopy techniques. Molecules 26, 1942.
Gunaydin, G., Gedik, M.E., Ayan, S., 2021. Photodynamic therapy-current limitations and novel approaches. Front. Chem. 9, 691697.
Hak, A., Ali, M.S., Sankaranarayanan, S.A., Shinde, V.R., Rengan, A.K., 2023. Chlorin e6: a promising photosensitizer in photo-based cancer nanomedicine. ACS Appl. Bio Mater. 6, 349–364.
Hasobe, T., Rabbani, M.G., Sandanayaka, A.S., Sakai, H., Murakami, T., 2010. Synthesis and aggregate formation of triphenylene core-centered porphyrin hexamers. Chem. Commun. (Camb.) 46, 889–891.
Huis In't Veld, R.V., Heuts, J., Ma, S., Cruz, L.J., Ossendorp, F.A., Jager, M.J., 2023. Current challenges and opportunities of photodynamic therapy against cancer. Pharmaceutics 15, 330.
Isakau, H.A., Trukhacheva, T.V., Petrov, P.T., 2007. Isolation and identification of impurities in chlorin e6. J. Pharm. Biomed. Anal. 45, 20–29.
Jeong, H., Huh, M., Lee, S.J., Koo, H., Kwon, I.C., Jeong, S.Y., Kim, K., 2011. Photosensitizer-conjugated human serum albumin nanoparticles for effective photodynamic therapy. Theranostics 1, 230–239.
Jia, C., Guo, Y., Wu, F.G., 2022. Chemodynamic therapy via Fenton and Fenton-like nanomaterials: strategies and recent advances. Small 18, e2103868.
Jo, J., Kim, J.Y., Yun, J.J., Lee, Y.J., Jeong, Y.I., 2023. B-Cyclodextrin nanophotosensitizers for redox-sensitive delivery of chlorin e6. Molecules 28, 7398.
Kim, G., Lee, Y.E., Xu, H., Philbert, M.A., Kopelman, R., 2010. Nanoencapsulation method for high selectivity sensing of hydrogen peroxide inside live cells. Anal. Chem. 82, 2165–2169.
Kim, H.J., Lim, Y.G., Song, Y.J., Park, K., 2023. Folate receptor-targetable and tumor microenvironment-responsive manganese dioxide-based nano-photosensitizer for enhancing hypoxia alleviation-triggered phototherapeutic effects. J. Ind. Eng. Chem. 119, 428–438.
Kim, T.E., Chang, J.E., 2023. Recent studies in photodynamic therapy for cancer treatment: from basic research to clinical trials. Pharmaceutics 15, 2257.
Lan, M.H., Zhao, S.J., Liu, W.M., Lee, C.S., Zhang, W.J., Wang, P.F., 2019. Photosensitizers for photodynamic therapy. Adv. Healthc. Mater. 8, e1900132.
Lee, S.H., Wu, H.Q., Yeo, S.H., Lee, W.K., Yoon, I., 2023. Transition metal-dependent heavy-atom effect of metallochlorin photosensitizers for enhanced photodynamic therapy. Inorg. Chem. Commun. 152, 110693.
Leshem, G., Richman, M., Lisniansky, E., Antman-Passig, M., Habashi, M., Graslund, A., Warmlander, S., Rahimipour, S., 2019. Photoactive chlorin e6 is a multifunctional modulator of amyloid-beta aggregation and toxicity via specific interactions with its histidine residues. Chem. Sci. 10, 208–217.
Liao, S., Cai, M., Zhu, R., Fu, T., Du, Y., Kong, J., Zhang, Y., Qu, C., Dong, X., Ni, J., Yin, X., 2023. Antitumor effect of photodynamic therapy/sonodynamic therapy/sono-photodynamic therapy of chlorin e6 and other applications. Mol. Pharm. 20, 875–885.
Lim, Y.G., Park, H.G., Park, K., 2025. Facile one-pot preparation of self-assembled hyaluronate/doxorubicin nanoaggregates for cancer therapy. Biomimetics (Basel) 10, 91.
Liu, J., An, T., Chen, Z.H., Wang, Z.Z., Zhou, H., Fan, T.X., Zhang, D., Antonietti, M., 2017a. Carbon nitride nanosheets as visible light photocatalytic initiators and crosslinkers for hydrogels with thermoresponsive turbidity. J. Mater. Chem. A 5, 8933–8938.
Liu, P., Xie, X., Shi, X., Peng, Y., Ding, J., Zhou, W.J.A.A.M., 2019. Oxygen-self-supplying and HIF-1α-inhibiting core–shell nanosystem for hypoxia-resistant photodynamic therapy. ACS Appl. Mater. Interfaces 11, 48261–48270.
Liu, P., Zhou, Y., Shi, X., Yuan, Y., Peng, Y., Hua, S., Luo, Q., Ding, J., Li, Y., Zhou, W., 2021. A cyclic nano-reactor achieving enhanced photodynamic tumor therapy by reversing multiple resistances. J Nanobiotechnology 19, 149.
Liu, Y., Shen, W., Li, Q., Shu, J., Gao, L., Ma, M., Wang, W., Cui, H., 2017b. Firefly-mimicking intensive and long-lasting chemiluminescence hydrogels. Nat. Commun. 8, 1003.
Ma, C.H., Yang, J., Mueller, J.L., Huang, H.C., 2021. Intratumoral photosensitizer delivery and photodynamic therapy. Nano Life 11.
Min, J.S., Hong, J.Y., Lim, Y.G., Ahn, J.W., Park, K., 2021. Oxygen-generating glycol chitosan-manganese dioxide nanoparticles enhance the photodynamic effects of chlorin e6 on activated macrophages in hypoxic conditions. Int. J. Biol. Macromol. 184, 20–28.
Nguyen, T.T., Nguyen, H.N., Nghiem, T.H.L., Do, X.H., To, T.T, Do, T.X.P., Do, D.L., Nguyen, H.G., Nguyen, H.M., Nguyen, N.D., Luu, M.Q., Nguyen, T.N., Nguyen, T.B. N., Nguyen, V.T., Pham, V.T., Than, U.T.T., Hoang, T.M.N., 2024. High biocompatible FITC-conjugated silica nanoparticles for cell labeling in both in vitro and in vivo models. Sci. Rep. 14, 6969.
Ocakoglu, K., Joya, K.S., Harputlu, E., Tarnowska, A., Gryko, D.T., 2014. A nanoscale bio-inspired light-harvesting system developed from self-assembled alkyl-functionalized metallochlorin nano-aggregates. Nanoscale 6, 9625–9631.
Pandit, R.P., Thapa Magar, T.B., Shrestha, R., Lim, J., Gurung, P., Kim, Y.W., 2024. Isolation, identification, and biological activities of a new chlorin e6 derivative. Int. J. Mol. Sci. 25, 7114.
Park, E.J., Song, J.W., Kim, H.J., Kim, C.S., Song, Y.J., Yang, D.H., Yoo, H., Kim, J.W., Park, K., 2020. In vivo imaging of reactive oxygen species (ROS)-producing pro-inflammatory macrophages in murine carotid atheromas using a CD44-targetable and ROS-responsive nanosensor. J Ind Eng Chem 92, 158–166.
Park, J.S., Kim, S.K., Choi, C.H., Park, J.P., Park, K., 2023. Novel chemiluminescent nanosystem for highly sensitive detection of hydrogen peroxide in vivo. Sensor Actuat B-Chem 393, 134261.
Pei, Q., Zhou, S.Y., Lu, S.J., Hao, D.Y., Xiang, X.J., Hu, X.L., Jing, X.B., Xie, Z.G., 2023. Ferric ion-driven chlorin e6 nanoparticles: simple and effective multimodal theranostics. Adv. Funct. Mater. 33, 2304205.
Qu, H., Chen, H., Cheng, W., Wang, Y., Xia, Y., Zhang, L., Ma, B., Hu, R., Xue, X., 2023. A supramolecular assembly strategy for hydrophilic drug delivery towards synergistic cancer treatment. Acta Biomater. 164, 407–421.
Rubab, A., Baig, N., Sher, M., Ali, M., Ul-Hamid, A., Jabeen, N., Khan, L.U., Sohail, M., 2022. Synthesis and characterization of a carbon-supported cobalt nitride nano-catalyst. Chemnanomat 8, e202100428.
Song, J.W., Ahn, J.W., Lee, M.W., Kim, H.J., Kang, D.O., Kim, R.H., Kang, U.G., Kim, Y. H., Han, J., Park, Y.H., Nam, H.S., Yoo, H., Park, K., Kim, J.W., 2021. Targeted theranostic photoactivation on atherosclerosis. J Nanobiotechnology 19, 338.
Song, Y.J., Kim, J.J., Sul, W.J., Park, K., 2024. Calcium carbonate particle platform for chemodynamic and self-luminescent photodynamic combination antibacterial therapy. J. Environ. Chem. Eng. 12, 111987.
Song, Z., Adeyemo, A.O., Baker, J., Traylor, S.M., Lightfoot, M.L., 2011. Structure of porphyrin Tpps(4) and its interaction with metal ions as elucidated by (1)H NMR and uv-visible spectra. Ga J Sci 69, 89–101.
Tian, H., Zhang, T., Qin, S., Huang, Z., Zhou, L., Shi, J., Nice, E.C., Xie, N., Huang, C., Shen, Z., 2022. Enhancing the therapeutic efficacy of nanoparticles for cancer treatment using versatile targeted strategies. J. Hematol. Oncol. 15, 132.
Van Berlo, D., Woutersen, M., Muller, A., Pronk, M., Vriend, J., Hakkert, B., 2022. 10% Body weight (gain) change as criterion for the maximum tolerated dose: a critical analysis. Regul. Toxicol. Pharmacol. 134, 105235.
Wei, F.M., Rees, T.W., Liao, X.X., Ji, L.N., Chao, H., 2021. Oxygen self-sufficient photodynamic therapy. Coordin Chem Rev 432, 213714.
Wen, H., Wu, Q., Xiang, X., Sun, T., Xie, Z., Chen, X., 2024. PEGylated BODIPY photosensitizer for type I dominant photodynamic therapy and afterglow imaging. ACS Appl. Mater. Interfaces 16, 61739–61750.
Yi, J., Liu, L., Gao, W., Zeng, J., Chen, Y., Pang, E., Lan, M., Yu, C., 2024. Advances and perspectives in phototherapy-based combination therapy for cancer treatment. J. Mater. Chem. B 12, 6285–6304.
Yu, H., Huang, Z., Wu, J., Zhao, Z., Hua, Y., Yang, Y., 2025. Chlorin e6: a promising photosensitizer of anti-tumor and anti-inflammatory effects in PDT. Nanomedicine (Lond.) 20, 389–400.
Zhang, C., Bu, W., Ni, D., Zhang, S., Li, Q., Yao, Z., Zhang, J., Yao, H., Wang, Z., Shi, J., 2016. Synthesis of iron nanometallic glasses and their application in cancer therapy by a localized Fenton reaction. Angew. Chem. Int. Ed. Engl. 55, 2101–2106.
Zhang, W., Hao, L., Huang, J., Xia, L., Cui, M., Zhang, X., Gu, Y., Wang, P., 2019. Chemiluminescence chitosan hydrogels based on the luminol analog L-012 for highly sensitive detection of ROS. Talanta 201, 455–459.
Zou, J., Zhu, J., Yang, Z., Li, L., Fan, W., He, L., Tang, W., Deng, L., Mu, J., Ma, Y., Cheng, Y., Huang, W., Dong, X., Chen, X., 2020. A phototheranostic strategy to continuously deliver singlet oxygen in the dark and hypoxic tumor microenvironment. Angew. Chem. Int. Ed. Engl. 59, 8833–8838.